An FDEM study of particle breakage under rotational point loading

Deheng Wei,[1] Budi Zhao,[2] Daniel Dias-da-Costa[1,3] and Yixiang Gan[1 *]

[1]School of Civil Engineering,
The University of Sydney, Sydney, Australia

[2] Department of Earth Science and Engineering,
King Abdullah University of Science and Technology, Thuwal, Saudi Arabia

[3]ISISE, Department of Civil Engineering,
University of Coimbra, Portugal

*Corresponding author: Dr. Yixiang Gan
yixiang.gan@sydney.edu.au

[*] Corresponding author. Email: yixiang.gan@sydney.edu.au

Nomenclature

c_n^m	Spherical Harmonic coefficients of degree *n* and order *m*
D	damage variable for linear damage evolution
D'	damage parameter
d	particle size
E	elastic modulus
E_i, E_k, E_D, E_E, E_S, E_W and E_F	internal, kinetic, damage, elastic, strain, input and friction energies
F_max	particle breakage force
$\mathbf{F}_e$ and $\mathbf{F}_i$	external and internal forces
G_C	critical fracture energy
$G_{n,C}$ and G_{shear}	critical fracture energies for failure in the normal and shear directions
$\mathbf{K}$	elasticity matrix
k_1, k_2, k_M and k_g	maximum, minimum, average and Gaussian curvature values
k_C and k_com	curvedness and combined curvedness
k_n, k_s and k_t	CIE stuffiness along normal, the first and second shear directions
L_{min}	minimum mesh size
$\mathbf{M}$	diagonal mass matrix
N_max, S_max and T_max	failure stresses towards normal, the first and second shear directions
R^*	relative contact radius of the Hertzian contact model
R_1 and R_2	radius of two contacted spheres
$r_i(\theta, \varphi)$	distance between the mass canter and *i*-th point on particle surface
T	thickness of cohesive elements
t	time
u, $\dot{u}$ and $\ddot{u}$	displacement, velocity and acceleration
$\ddot{\mathbf{u}}$	acceleration vector
V	particle volume
$\boldsymbol{Y}_n^m(\theta, \varphi)$	Spherical Harmonic functions of latitudinal coordinate θ and longitudinal coordinate φ
$\boldsymbol{\sigma}$	nominal traction stress vector
$\boldsymbol{\sigma}^c$	stress from overall constitutive equation of particle
$\boldsymbol{\sigma}^u$	undamaged stress
σ_f	particle breakage or failure stress
σ_n, σ_s and σ_t	stresses towards normal, the first and second shear directions
σ_eff^0	effective traction stress
$\boldsymbol{\delta}$	displacement matrix
δ_n, δ_s and δ_t	displacements towards normal, the first and second shear directions
δ_m^0 and δ_m^{sep}	displacements for crack initiation and complete failure of CIEs
ε	strain
$\dot{\varepsilon^{el}}$	elastic strain rate
ρ	density of bulk material
η	material parameter for the Benzeggagh-Kenane criterion
χ	energy-based mode mixed ratio
μ	friction coefficient
Δt	time step

Abbreviations

CIE	Cohesive interface element
LBS	Leighton Buzzard sand
XCT	X-Ray computed tomography

An FDEM study of particle breakage under rotational point loading

Deheng Wei,[1] Budi Zhao,[2] Daniel Dias-da-Costa[1,3] and Yixiang Gan[1] †

[1]School of Civil Engineering, The University of Sydney, Sydney, NSW 2006, Australia

[2] Department of Earth Science and Engineering, King Abdullah University of Science and Technology, Thuwal, Saudi Arabia

[3] Department ISISE, Department of Civil Engineering, University of Coimbra, Portugal

Abstract

The most commonly adopted method to test the strength of single sand particles is based on platen experiments. This setup tends to align the loading direction towards the particle minimum axis and provide an upper limit for the breakage stress. This paper numerically bypasses such limitation by using a combined finite and discrete element method (FDEM). FDEM was first validated via a mesh size analysis of a spherical particle and calibrated by in-situ experimental compressions of the single quartz sand particle, where the particle shape was obtained by X-ray micro-computed tomography (XCT) and then imported into the numerical model. Systematic point loading tests were recreated to explore the role of the curvature at contacting points on the breakage behaviour. The simulations allow to probe the same non-spherical particles, i.e., realistic quartz sand and ellipsoid particles, with multiple measurements highlighting the importance of the loading direction, which was inaccessible experimentaly. Results

† Corresponding author. Email: yixiang.gan@sydney.edu.au

show that FDEM can capture not only the crack initiation but also fracture patterns, while taking into account realistic shapes. It is found that the distance between two contact points and their combined curvedness reflecting the particle morphology are the two major factors governing fracture patterns and stresses. When loading is roughly parallel to the minimum principal dimension of particles, the obtained breakage stress and the number of fragments approach the upper limits.

Keywords: Particle breakage; point loading; FDEM; computed tomography; crack initiation; crack evolution; fracture patterns

Highlights

i) An FDEM benchmarked with XCT was used to simulate particle breakage focusing on shape effects.

ii) Rotational point load simulations probed the same non-spherical particle breakage.

iii) Breakage stress and patterns are governed by loading distances and the curvature of contact points.

iv) Maximum stored elastic energy during deformation can be an effective breakage criterion.

1. Introduction

The micromechanical understanding of particle breakage targeting particle morphology, size and packing structure, bulk material properties and loading conditions is sought-after in an extensive range of applications including granular materials, soil mechanics, geology, and across the broader field of engineering [1-3]. Due to the difficulty in quantifying particle morphology features, particle size is usually taken as a first-order approximation for correlating breakage behaviours. There are two types of models considering size effects in the strength of material and structure design: deterministic size effect based on stress redistribution and released energy, e.g., un-notched size effect law [4-5]; and statistical size effect considering material defects, e.g., using Weibull distribution [6-7].

Stress-induced single particle breakage associated with its morphology features is of fundamental importance in geotechnical applications including blast loading, pile driving and large rockfill dams. Methods to study single particle strength or breakage can be classified into three categories: experimental [7-8], analytical [9-11] and numerical [12-14] approaches.

In the experimental approach, due to the small size of sand particles, nearly all 1D compression tests to measure individual particle strength through flat platen loading, where a single particle is compressed between two flat rigid platens. Displacement and force at the loading platen on the particle are simultaneously recorded. Point loading, widely applied for large-sized rock blocks [15], is a more realistic testing method, since most contacts inside granular assemblies are point-to-point rather than point-to-flat-

face contacts. Based on point load tests, most analytical methods [16-17] are conducted with the assumption of hard-soft contacts between load caps and spherical particles. In fact, the mechanical properties of compressing platens govern the breakage behaviour of the quartz sphere via the ratio between contacting radius (a) and sphere radius (R).For low ($a/R<0.3$), intermediate ($0.3<a/R<0.65$) or high ($a/R>0.65$) contact radius, the corresponding particle breakage occurs just outside the contact perimeter, near the sphere centre, or along the particle equator due to the shift of maximum tensile stress [18]. Apparently, the location of fracture initiation is hard to detect experimentally even though necessary to bridge analytical solution and experiments. From the analytical solution of Russell and Wood [19], the breakage occurs just below contacting points and is driven by shear stresses, which have been qualitatively reflected by many small fragments below contacting area. This has been captured by the X-ray micro computed tomography (CT) images [20]. Zhu and Zhao [21] simulated the compression of a single sphere particle using peridynamics and found the fracture pattern to be similar to the experimental breakage behaviour of an LBS particle with the so-called good roundness contact point in Zhao et al. [20]. However, such peridynamics simulations did not reproduce the typically observed small shear-induced fragments near contact areas.

When platen loading tests are applied for irregular-shaped particles, the most used equation for calculating irregular particle strength is taken from the analytical and experimental approach of point load tests in [16]: $\sigma_f = F/d^2$, where F is the breakage force, σ_f is the breakage stress, and d is the distance between the two contact points at the particle surface in point load tests. It should be highlighted that if the particle,

particularly of non-convex shape, is laid on a bottom platen, at least three contact points would theoretically develop, either macroscopic or at asperity level contact points, on the bottom platen and more than one contact point with the upper platen, although during the consequent loading process of the compressed particle the contact points may vary. Therefore, occasionally the extremely non-spherical particle does not endure purely compressive loading but also structural bending, which may hinder the extended use of the simplified equation in the analysis.

Regardless of the difficulties in quantitatively correlating particle morphology, in terms of shape parameters and curvature of contact points, there are experimental investigations on single particle breakage behaviour in 1D compression that can be highlighted. Zhao et al. [20] found the stress concentration to occur at contact points with high curvature via X-ray CT, which was also observed by Wang and Coop [8]. Cavarretta et al. [22] discussed the relevance of roundness from 2D curvature to particle crushing strength and concluded that rounded particles can endure high loaded stress due to the increased possibility of larger contact radii. Brzesowsky et al. [23] polished the bottom of crushing irregular particles to discover the relation between the curvature of only one contact point touching the top platen and breakage force for simplification. However, the curvature values in their experiments were based on one or several randomly selected 2D particle projections, which may not be sufficiently representative in 3D. Therefore, they found no obvious quantitative relation between particle breakage stress and curvature index.

A complementary tool to investigate particle breakage behaviour can be based in

computational mechanics. Discrete element method (DEM) is currently the most often adopted in the context of geotechnical engineering for sand particles. Two main approaches for handling particle breakage can be identified: one is based on bonded clusters, where a particle is composed of bonded small sphere elements [12-13, 24-25]; and another approach replaces a 'broken' particle with a few smaller spherical particles [26-28]. Unfortunately, both approaches lack rigorous theoretical basis of fracture mechanics at the particle scale. In recent years, the development of 3D X-ray micro-tomography and laser techniques for accurate reconstruction of sand particle surfaces opened the possibility for simulating realistic particle morphology with computational models, such as the granular element method (GEM) [29] and level set DEM (LS-DEM) [30-31]. The finite element method (FEM) with surface meshes is more suitable for depicting realistic particle morphology when compared with other DEM-based computational tools [32]. Druckrey and Alshibili [33] implemented the extended finite element method (XFEM) to simulate the 1D compression of single quartz sand particles based on in-situ X-ray synchrotron images. However, due to the features of the enriched elements used to simulate smeared fracture and difficulties in handling differences in density within the particle, only one flat fracture surface connecting two loading areas could develop, which may be insufficient for capturing the fracture patterns found in experiments and including four typical modes, namely major splitting, explosive, chipping and mixed modes [8].

In this study, a combined finite and discrete element method (FDEM) approach is adopted to simulate particle breakage behaviour, via multi-directional two-point

loading, focusing on the particle shape effects. The simulations of rotational point loading provide a unique advantage since it allows probing the same non-spherical particle shapes with multiple breakage measurements assessing the role of loading direction, which is inaccessible in experiments. The paper is organised as follows. In Section 2, the FDEM approach is introduced and benchmarked with XCT-monitored experiments. In Sections 3 and 4, spherical quartz particles are simulated with variant relative contact radius, to bridge breakage behaviour and curvature values of contact points. Rotational loading simulations of the XCT scanned particle and ellipsoid are also conducted and analysed, revealing that particle breakage behaviour, regarding breakage stress and fracture patterns, is governed by both their loading distance and the curvature of contact points. Further analyses show that the maximum stored strain energy during deformation can be an effective breakage criterion to determine brittle particle strength. Finally, the main conclusions are summarised in Section 5.

2. Combined finite and discrete element method

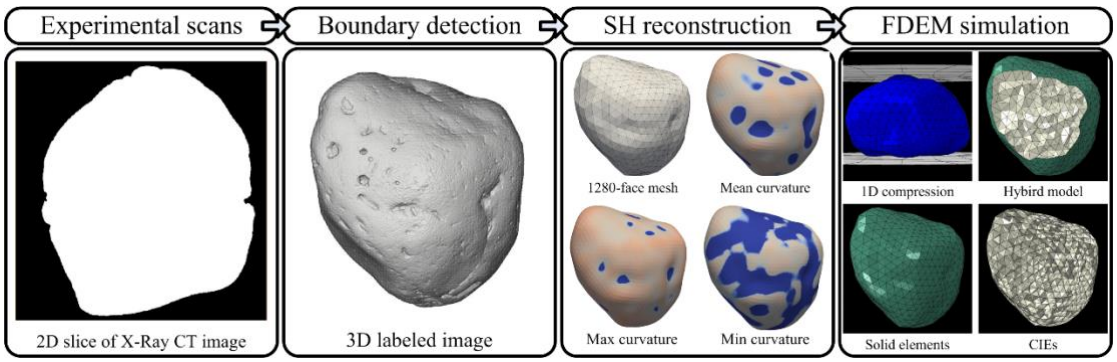

Fig. 1 From experimental in-situ X-ray computed tomography to FDEM simulation of particle breakage behaviour using platen loading

FDEM combines FEM with contact detection and interaction to simulate not only the continuum behaviour within the particle but also the initiation and development of internal cracks and the interactions between fragments. Abaqus/Explicit [34] is herein adopted for developing the FDEM simulations given its ability to deal with a large number of contacts between discontinuous elements undergoing large deformation.

2.1 Image processing and mesh generation

Fig. 1 shows a typical workflow for preparing our FDEM simulations of single particle crushing considering realistic particle shape. There are four steps: (1) the CT-monitored experiment for an LBS particle in [20] offering a series of X-Ray raw CT images during platen loading; (2) extraction of 3D voxel-based particle shape using image processing; (3) reconstruction of particle morphology with Spherical Harmonic analyses; and (4) discretization into 3D tetrahedron meshes for FDEM simulation.

The 3D CT data can be visualised as a stack of 2D images, each with a cross-section of the scanned sample with the thickness of one voxel of high resolution of 3.3 μm. The image processing and scanning from CT-monitored sets of 2D slice images to reconstruct the particle mesh is done following the procedure described in [20]. The main steps include the use of a 2D median filter [35] to reduce the noise on every slice, then followed by binarization of the filtered image for detection of the LBS particle boundaries from distinct material phases. The labelled CT images are smoothed using spherical harmonics (SH) in polar coordinates by decomposing a spherical scaler function as follows [36]:

$$r_i(\theta,\varphi)=\sum_{n=0}^{\infty}\sum_{m=-n}^{n}c_n^m Y_n^m(\theta,\varphi)\ , \tag{1}$$

where i denotes i-th points on CT-based particle surface; r is the distance between surface points and particle mass centre; $\boldsymbol{Y}_n^m(\theta,\varphi)$ and c_n^m are the SH functions and coefficients at degree n and order m defined in [37], respectively; and $\theta \in [0,\pi]$ and $\varphi \in [0,2\pi]$ are the latitudinal and longitudinal coordinates.

To perform rotational point load tests for the same particle, of which only vertices of triangular meshes contact with load point ends, the selected surface point ($r_i(\theta,\varphi)$) have a corresponding point ($r_j(\pi-\theta,\varphi+\pi)$) and the mass centre is on the line connecting them, as in Fig. 2. Finally, the generated surface mesh is converted into tetrahedron-composed solid domain [38].

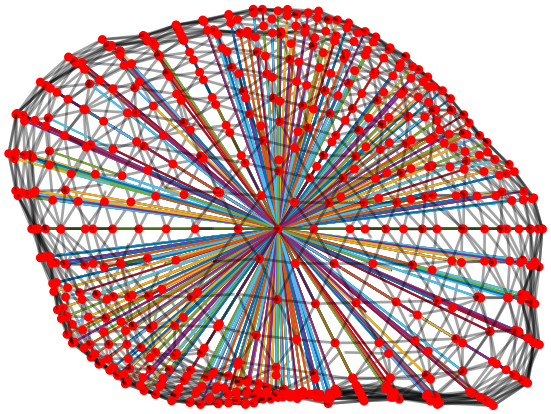

Fig. 2 The 'diameters' connecting the centre-of-mass and the vertices on particle surface

2.2 Model description

A particle is herein discretised in the context of FDEM by 4-node solid tetrahedron elements connected by zero thickness cohesive interface elements (CIEs in Fig. 1). The

tetrahedron elements are adopted for their compatibility with the triangular surface mesh reconstructed from CT images. The interface elements connect the adjacent solid elements until fracture initiation conditions are met. Fragments are generated when a throughout fracture plane develops. To allow for the multiple possibilities of fracture propagation, the tetrahedron elements need to be small enough. Following standard FEM principles, the nodal matrix for a moving element is governed by the following equilibrium equation:

$$\mathbf{M}\cdot\ddot{\mathbf{u}}+\mathbf{F}_i-\mathbf{F}_e=\mathbf{0}\ , \tag{2}$$

where $\ddot{\mathbf{u}}$ is the acceleration vector, $\mathbf{M}$ is the diagonal mass matrix and $\mathbf{F}_i$ and $\mathbf{F}_e$ are internal and external forces. $\mathbf{F}_i$ is composed of elastic force from isotropic solid tetrahedron elements and intact CIEs; $\mathbf{F}_e$ is resulted from the external contacts between particle and platens or between newly generated fragments.

A penalty formulation is used for contact with a tangential friction coefficient (μ=0.5) between fractured solid elements, and between solid elements and rigid platens . An explicit solver is adopted to obtain the solution via central difference integration framework, due to its higher efficiency in dealing with large number of contact and deformation when compared to implicit solvers. During the explicit integration scheme,

$$\dot{u}_{n+1/2}=\dot{u}_{n-1/2}+\frac{\Delta t_{n+1}+\Delta t_n}{2}\ddot{u}_n \tag{3}$$

$$u_{n+1}=u_n+\Delta t_{n+1}\dot{u}_{n+1/2} \tag{4}$$

$$\Delta t=\sqrt{\frac{\rho}{E}}L_{\min} \tag{5}$$

where u is a freedom degree, n means n-th time step or increment, and Δt denotes time

step; ρ is the density of bulk material, E is the elastic modulus, and $L_{\min}$ is the minimum length of mesh size. For the balance between computation efficiency and accuracy, mesh size should be selected carefully and will be discussed hereafter.

2.3 Damage model

Fracture or breakage is herein simulated by the failure of geometric zero-thickness cohesive elements using traction-separation damage laws [39-41]. The relationship between displacement and traction force at the cohesive zone follows the bilinear function, as stated in Fig. 3:

$$\boldsymbol{\sigma} = \begin{pmatrix} \sigma_n \\ \sigma_s \\ \sigma_t \end{pmatrix} = \mathbf{K}\boldsymbol{\delta} = \begin{pmatrix} k_{nn} & k_{ns} & k_{nt} \\ k_{sn} & k_{ss} & k_{st} \\ k_{tn} & k_{ts} & k_{tt} \end{pmatrix} \begin{pmatrix} \delta_n \\ \delta_s \\ \delta_t \end{pmatrix}, \tag{6}$$

where $\boldsymbol{\sigma}$ is the traction stress vector, $\mathbf{K}$ is the elasticity matrix, $\boldsymbol{\delta}$ is the relative displacement matrix, and n, s and t denote the normal and two shear directions. Off-diagonal components of the elastic matrix $\mathbf{K}$ are set to zero. The relative displacements are defined as:

$$\delta_{n,s,t} = \varepsilon_{n,s,t} T, \tag{7}$$

where ε is the strain along the three directions for the CIEs and T is the fictitious thickness herein set as 1 for the equality of nominal strain to its corresponding displacement [42-43].

The constitutive response of the CIEs covers two main stages, i.e., before and after breakage initiation. The maximum nominal stress criterion is applied to identify the breakage initiation in quartz sands as suggested in [33, 38]:

$$MAX\left\{\frac{\langle\sigma_n\rangle}{N_{\max}},\frac{\sigma_s}{S_{\max}},\frac{\sigma_t}{T_{\max}}\right\}=1$$

$$\langle\sigma_n\rangle=\begin{cases}\sigma_n,\ for\ \ \sigma_n\geq 0\\ 0,\ for\ \ \sigma_n\leq 0\end{cases}, \tag{8}$$

where $N_{\max}$, $S_{\max}$ and $T_{\max}$ are the failure stress of CIEs. Compressive stress is set to 0 to evaluate crack initiation criterion since compression is not considered as a source of breakage at micro-scale.

After crack initiation, contact stiffness reduces according to partial interface damage, and the stress-displacement relationship is updated by (Fig. 3):

$$\begin{aligned}&\sigma_n=\begin{cases}k_n\delta_n & for\ \ \delta_n\geq 0\\ k_n^0\delta_n & for\ \ \delta_n\leq 0\end{cases}\\ &\sigma_s=k_s\delta_s\\ &\sigma_t=k_t\delta_t\end{aligned}, \tag{9}$$

where $k_{n,s,t}=(1-D)k_{n,s,t}^0$. D is the damage variable for linear damage evolution defined as:

$$\begin{aligned}&D=\frac{\delta_m^{sep}(\delta_m^{\max}-\delta_m^0)}{\delta_m^{\max}(\delta_m^{sep}-\delta_m^0)}\\ &\delta_m^{sep}=\frac{2G_C}{\sigma_{eff}^0}\end{aligned}, \tag{10}$$

where δ_m^{sep} and δ_m^0 are the corresponding displacements for complete failure and crack initiation, and $\delta_m^{\max}$ is the maximum displacement registered during the loading history, σ_{eff}^0 ($=\sqrt{\langle\sigma_n\rangle^2+\sigma_s{}^2+\sigma_t{}^2}$) is the relatively effective traction stress at crack initiation, and G_C is the Griffith fracture energy for crack evolution.

The Benzeggagh-Kenane criterion [44] is used to consider the mixed mode opening:

$$\begin{aligned} G_C &= G_{n,C} + (G_{s,C} - G_{n,C})\left(\frac{G_{shear}}{G_T}\right)^{\eta} \\ G_{shear} &= G_s + G_t \\ G_T &= G_n + G_s + G_t \end{aligned}, \tag{11}$$

where $G_{n,C}$ and G_{shear} are the relatively critical energies for pure mode I (tension) and combination of mode II and mode III (shear), η is a material parameter, and G_T is the mixed fracture energy for CIEs.

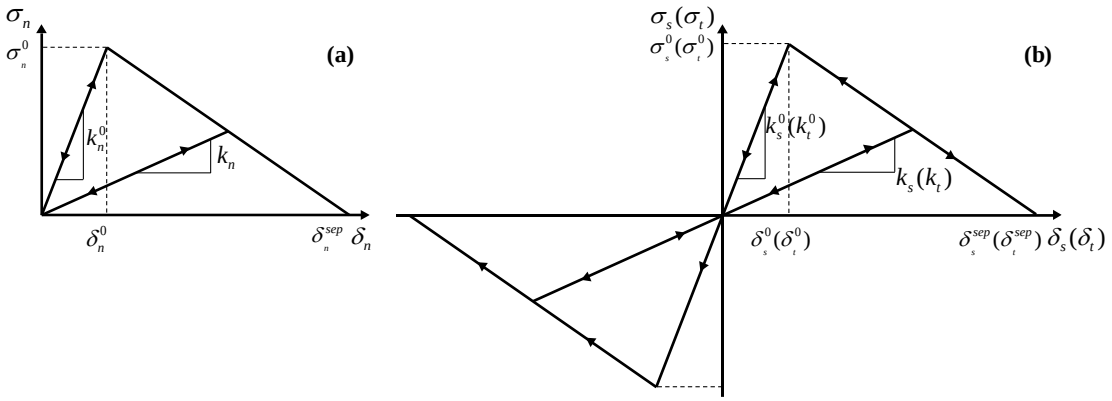

Fig. 3 Bilinear constitutive relations of CIEs: (a) Normal component; (b) Shear components

An energy-based mode mixed ratio is defined to detect the dominant type of damage during breakage:

$$\chi = 1 - \frac{G_n^{'}}{G_n^{'} + G_s^{'} + G_t^{'}}, \tag{12}$$

where G_n', G_s' and G_t' are the fracture energy done by tractions along corresponding displacements of normal, first and second shear directions, respectively. Accordingly, χ

is set to -1 before crack initiation. χ =0, χ =1 and 0 < χ <1 denote pure tension damage, pure shear damage and mixed damage modes, respectively. When defined during crack evolution or at crack initiation, χ varies or remains constant with time at an integration point.

Table. 1 summarises the main parameters obtained from the previous publications for quartz. These include the measurable physical parameters of quartz sand particle including density (ρ), elastic modulus (E), Poisson's ratio (υ), tensile strength (N_{max}) and shear strength (S_{max} and T_{max}) (Alshibili et al., 2013) and CIE stiffness (k_n, k_s and k_t), fracture energy (G_n, G_s and G_T) and material parameter (η) and their calibration process in FDEM [45-47]. The selection of adequate mesh size is key to accurately represent the fracture initiation and fracture energy; the element size should be less than the length of fracture propagation zone (FPZ). A rough estimation of the length of FZP was done following [45]. Then according to [71-72], a mesh size sensitivity study can be more targeted for the accuracy representation of fracture path.

	Parameter	Value
Solid elements	Density, ρ (kg/m^3)	2650
	Elastic modulus, E (GPa)	94.4
	Poisson's ratio, υ	0.118
Cohesive interface elements (CIE)	Normal stiffness, k_n (N/m^3)	9.44×10^{13}
	First shear stiffness, k_s (N/m^3)	4.22×10^{13}
	Second shear stiffness of, k_t (N/m^3)	4.22×10^{13}
	Tensile strength, N_{max} (MPa)	25.3
	First shear strength, S_{max} (MPa)	12.6
	Second shear strength, T_{max} (MPa)	12.6
	Mode I fracture energy, G_n (N/m)	100
	Mode II and III fracture energy, G_s and G_t (N/m)	200
	Material parameter, η	2
Contact law	Friction coefficient, μ	0.5

Table. 1 FDEM material parameters of quartz sand particles

2.4 Validation of FDEM in simulation particle breakage behaviour

2.4.1 Mesh sensitivity analysis

It has been widely known that mesh size significantly influences the mechanical behaviour in FEM-based simulation, hence the first part of study focuses on the analysis of a spherical particle with a diameter of 1.0 mm, which is close to the size of a realistic LBS particle. The material parameters are identical to the ones shown in Table. 1. The flat loading caps much harder than particles are used here for the mesh sensitivity study. To keep the quasi-static loading condition as in the experiments of [20], the loading speed in computational simulations has been checked to attain enough efficiency while keeping kinetic energy below 10% of its associated internal energy at the same time step. The upper platens ramp up to 0.2 m/s to stably introduce the contact between particle and two caps.

Fig. 4 illustrates the Mises stress distributions of 4 spheres just before breakage. Coarser mesh size results in less CIEs along which fracture surfaces can propagate thus generates simpler failure patterns. Finer meshes can alleviate this problem, meanwhile there is no obvious difference in stress distribution when the mesh size is sufficiently small (e.g., less than 0.075 mm).

The force-displacement curves of sphere simulations are shown in Fig. 5 (a), where convergence is observed with mesh size below 0.075 mm, although the 0.0375 mm mesh results in slightly higher peak force and displacement at failure. It should be noted that for the smaller mesh size, the local contact area with the platens

increases, contributing to the higher failure stress. Meanwhile the number of fractured CIEs increases, resulting in more potential crack paths, as compared with the courser mesh cases. This is attributed to the possible reason why variation of the displacement at failure is observed whilst the forces are nearly close to each other during loading process. A mesh refinement at contact area could be helpful in future simulations. The mesh size 0.075 mm corresponds to to 1,280 triangular surface elements, about 7,000 4-node solid elements and 20,800 6-node CIEs. To balance the simulation cost and accuracy, 1280 triangular surface meshes are used in all following simulations. Fig. 5 (b) illustrates the evolution of kinetic energy and internal energy during loading, inferring that the maximum ratio of kinetic energy to associated internal energy is less than 0.1, hence the loading rate is appropriate for representing quasi-static simulations. Notably, for platen loading on spherical particles, despite the main breakage observed, there are still remaining parts, particularly for fine-meshed particles, that are further compressed. Therefore, the internal energy continues to increase. Furthermore, fine meshes can induce larger maximum internal and kinetic energies.

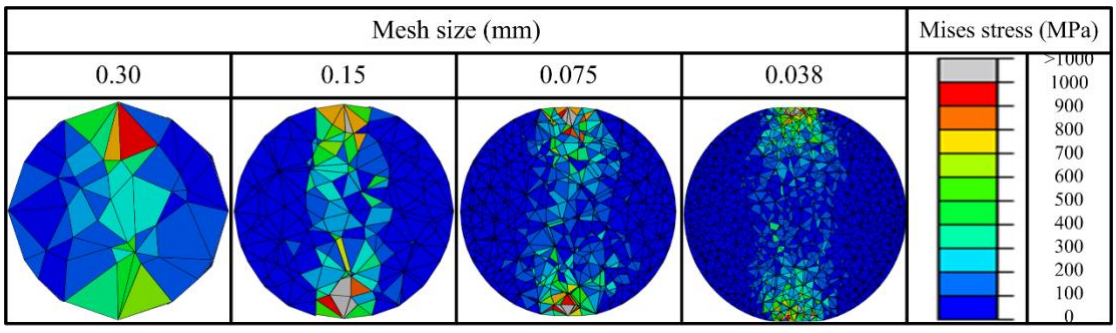

Fig. 4 The Mises stress distributions before the peak force for the spheres discretised with various mesh sizes

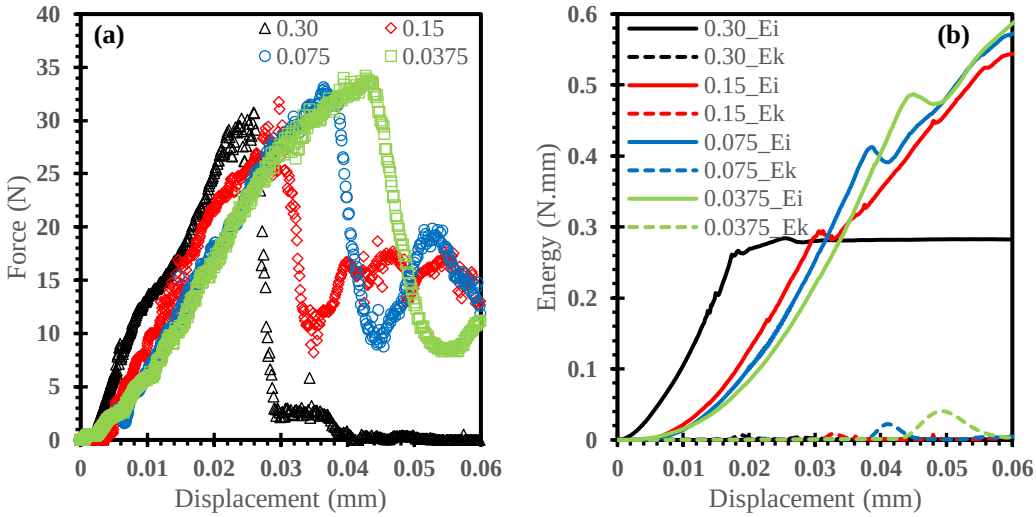

Fig. 5 Load-displacement curves (a) and the evolution of internal (E_i) and kinetic energies (E_k) (b) for the spheres discretised with different mesh sizes

2.4.2 Simulation of CT monitored platen loading test of a single LBS particle

The model is further validated by simulating an experimental single crushing test schematically shown in Fig. 1. The implemented particle shape was taken at the first CT scan with a prestressed state of a force of around 12.8N between two platens. In the experiment, this placement of the particle can bypass redundant rotation and sliding due to complexity of contact interactions, in particular within the low loading range. Please note that the loading platens in our experiments (with a cylindrical shape of radius 5 mm and height 5 mm) are made of ceramics with high Young's modulus (380 GPa) and low Poisson ratio (0.22), which is closer to rigid properties than steel (with Young's modulus and Poisson ratio about 200 GPa and 0.3) as used in other relevant studies. Furthermore, the size of loading platens is much larger than that (about 1 mm) of particle. For FEM-based simulations, the mesh size of two different contacting elastic

parts should have similar mesh size. If realistic platens were to be considered, a significantly heavy computational burden would be obtained. However, there is no significant difference in load-displacement curve and peak forces between cases with the rigid and elastic properties. Fig. 6 (a) shows the load-displacement curves for both simulation and experiment. Even though there are some differences regarding the peak load, which could be attributed to uncontrolled factors including differences of the platen, i.e., elastoplastic material in experiments and rigid platen used in simulations, mesh size, parameter selection, CIE model, and influence of preload on the shape of the scanned particles, it is worth noting that the curves are in a good agreement both in the elastic stage and after the first load drop. Furthermore, considering the resolution of CT images, Fig. 6 (b) plots the accumulative number N ($>d$) of 60 largest fragments versus their equivalent-volume diameters (d) in log-log scales. As found in previous studies [48-49], both experimental and simulated results shown here follow fractal relationships, $N \sim d^{-D}$, where D is the fractal dimension. The largest 6 fragments are significantly close, which proves the ability of the model in capturing the particle breakage behaviour, even if no internal inhomogeneity was included in the simulation. Although the smaller fragment size is highly dependent on the mesh size, the fractal dimension (1.542) from simulation results is still within the typical range for sand when compared with that (1.475) of relative in-situ CT experiments. In addition, higher values in the range of $1.77 < D < 3.06$ in FDEM studies [71-72] has been found for impact-induced single particle breakage behaviour.

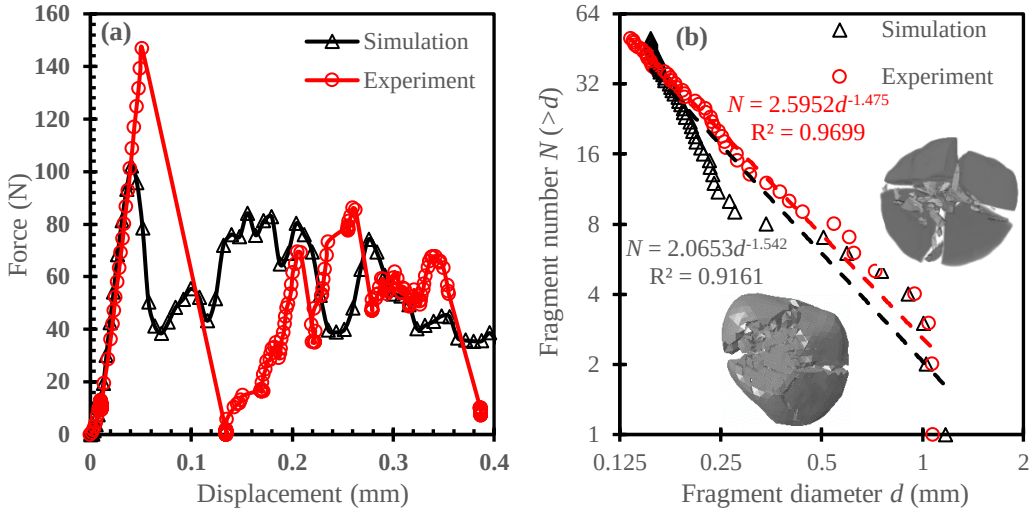

Fig. 6 Comparison of results for simulated and experimental 1D compression tests of single particle using flat platen: (a) Load-displacement curves; (b) Fractal distribution of fragment volume-equivalent sizes with two snapshots for the simulation (the left) and experiment (the right) at 0.135 mm displacement

3. Modelling diametral point load tests

In this section, traditional point load tests are applied to study the relations between particle breakage behaviour (e.g., breakage stress and fracture patterns) and particle morphology features (e.g., loading distances and curvature at contact points). The relation, $\sigma_f = F/d^2$, here used to calculate the breakage stress, is more suitable for point load tests and, since only pure compression forces are considered, deformation from bending moment needs to be excluded. The loading distances (d) are the 'diameter' connecting two load points; whereas the curvature values are quantified at the contacting vertices of the 3D surface meshes. Crushing of spherical and non-spherical particles is addressed here: spherical particles are compressed for validation of the analytical solution and studying the relation between breakage behaviour and curvature

at contacting areas; and CT-scanned realistic-shaped and ellipsoid particles are compressed at variable diametrical positions via rotation of the loading caps to consider not only the effects of the contact curvature, but also of load distances. Furthermore, the fracture patterns are categorised by the number of main fragments.

3.1 Spherical particle breakage behaviour

To assess the differences in particle breakage behaviour between point and platen loadings, the study starts with spherical particles since they have constant curvature regardless of the point considered over the surface. Three equal-mesh-sized spheres with radius 0.5 mm, 0.75 mm and 1.0 mm are compressed diametrically by two equally-sized rigid spheres as shown in Fig. 7. All material properties, as well as the friction coefficient, are taken from Table. 1. Fig 8 shows for one compressed spherical particle how its breakage or failure stress σ_f is significantly correlated with the relative contact radius (R^*) in the Hertzian contact model, defined as:

$$\sigma_f = \frac{F_{\max}}{d^2} \tag{13}$$

$$\frac{1}{R^*} = \frac{1}{R_1} + \frac{1}{R_2} \tag{14}$$

where $F_{\max}$ is the maximum force applied on the particle during the compression process, d is the distance between two contact points, and R_1 and R_2 are the radiuses of each contacting sphere. For one sphere, there are seven simulations considering various rigid sphere radius including 0.1, 0.2, 0.4, 0.8, 1.6, 3.2 mm and ∞ (i.e., flat platen), of which surfaces are always composed of 5,120 triangular elements.

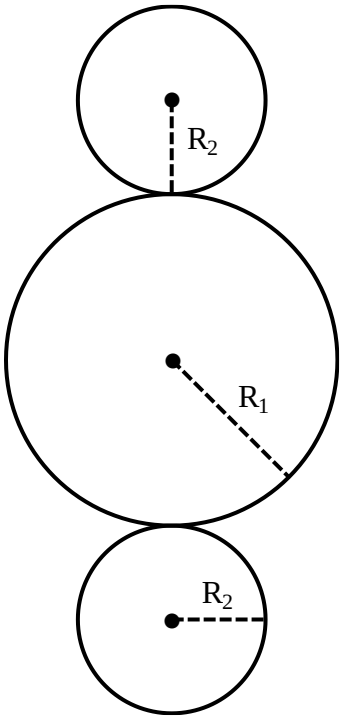

Fig. 7 The 2D representation of point load tests for various sized spherical particles

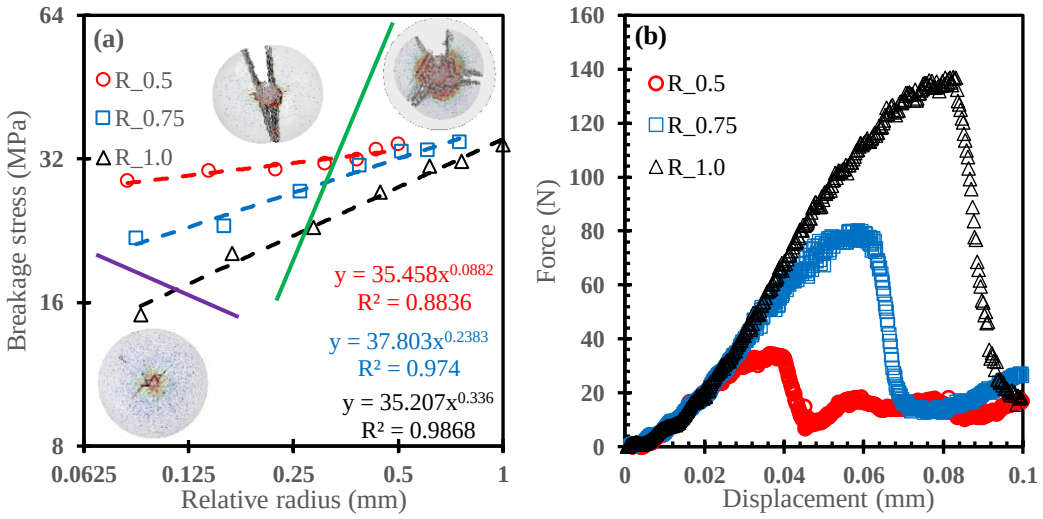

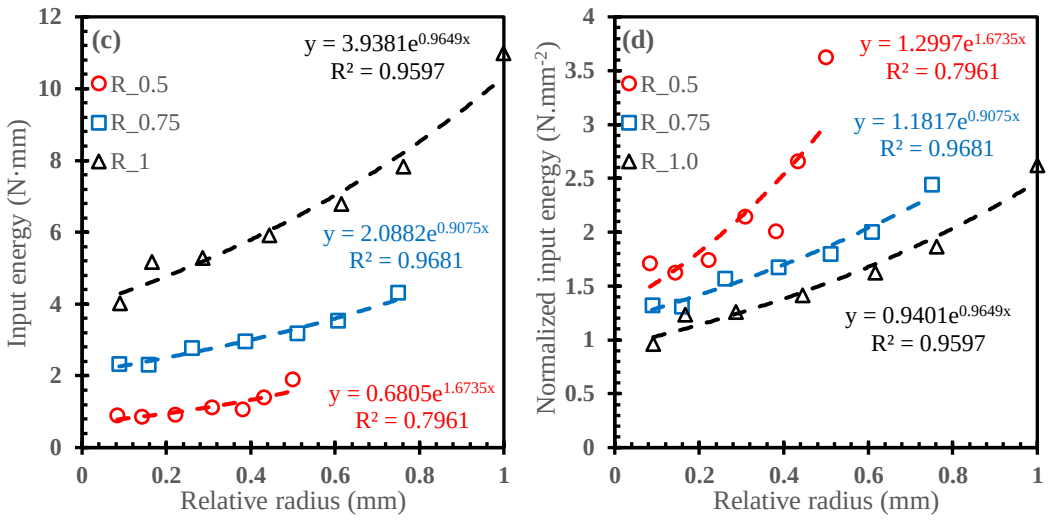

Fig. 8 Breakage of spherical particles: (a) Correlation between breakage stress and relative radius for different sized spheres (the solid lines represent approximate dividing lines for three different failure modes: no main fragments, two main fragments and three main fragments.), (b) load-displacement curves for platen compression, (c) relationship between input energy and relative radius, and (d) relationship between input energy normalized by particle volume and relative radius. (R_0.5 means the sphere with radius of 0.5 mm).

The linear relations between breakage stress and relative radius in the log-log scale are observed in Fig. 8 (a), showing that the particle breakage is sensitive to the stress concentration at the contact points. Therefore, it would be expected that the commonly adopted maximum stress criteria should depend on the local contact curvature. Another obvious tendency is the equivalent breakage stresses for the three sphere particles when compressed by platens, as illustrated in Fig. 8 (b) showing no size dependency since the simulations did not include any micro-flaw distributions. By eliminating material inhomogeneities from the analysis, focuses can be given to the influence of the particle

shape alone on the breakage behaviour. As the mesh size of the three different-sized spheres is the same, for large sized particle more CIEs need to be fractured, hence requiring more energy and fracture force, as in Fig. 8 (b) and (c). With decreasing contact curvature, the spherical particle would split into more major fragments. This phenomenon is associated with the stored energy which is required at breakage to generate the fracture surfaces (Fig. 8 (c)), e.g., less force concentration and higher stored energy for cases with higher relative radii at the contact. In addition to generating two or three main fragments, when the curvature of the rigid sphere is much less than that of the breakable sphere, the small sphere would engrave into the larger sphere without major fragments, as illustrated in Fig. 8 (a). Interestingly, from the view of a deterministic model of input energy normalised by the particle volume [62], for the same particle, the volume-averaged energy is also high relevant to the relative contact radius, and the model is thus size independent, as in Fig. 8 (d).

As aforementioned, Russell and Wood [19] concluded that sphere breakage initiate just below the contact area, locally shear-induced and dependent on the maximum ratio of the second to the first stress tensor, denoted by a large number of small fragments underneath contact areas numerically (the fracture pattern of platen load in Fig. 8 (a)) and experimentally [20]. Even though Russell and Wood [19] conducted analytical modelling of single particle compression in the context of point loading, a uniform normal pressure is applied at contact area (see Fig. 3 of [19]), which is different from flat platen loading condition. As demonstrated by the defined mixed-mode ratio χ in Fig. 9, it is evident that not only the maximum-stress-based crack

initiation but also the energy-based crack evolution result from shear deformation, which is consistent with the analytical solution.

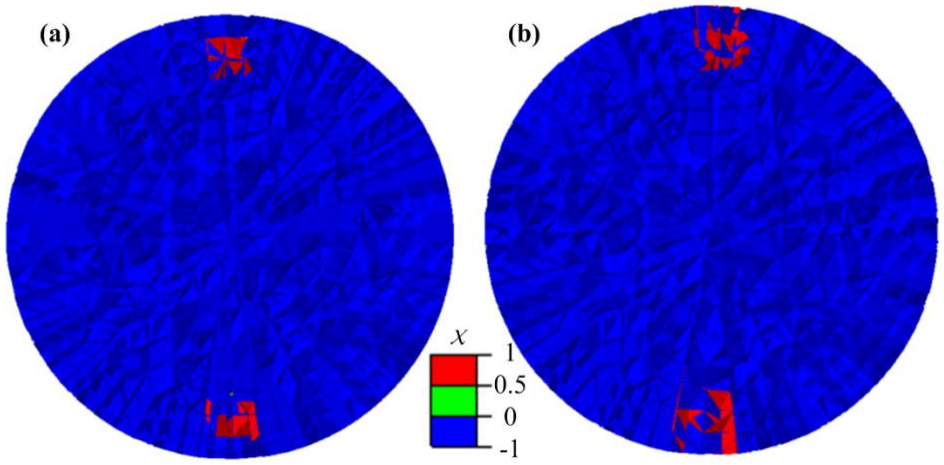

Fig. 9 Early breakage types of CIEs from platen loading: (a) crack initiation; (b) crack evolution (Red denotes shear dominant crack type)

3.2 Realistic particle shapes and fracture patterns

The traditional test method for assessing the single particle strength has a pre-step of letting the particle settle down by gravity onto the platen. This results in the particle alignment towards its minimum principal dimension. However, in a granular assembly, particle orientations tend to be rearranged frequently and the resulting contact force network can be rather complex. In the following, the single particle breakage behaviour under different diametrical loading conditions is investigated. The radius of curvature at point ends, similar to [50], is 0.2 mm and the height of the loading cap is 0.1 mm above all the corresponding displacements at breakage. The particle is rotated around

its centre-of-mass, as shown in Fig. 2. Using spherical harmonic reconstruction, vertex-vertex contacts, rather than vertex-face contacts, between rigid and breakable parts can be obtained before particle breakage, thus avoiding difficulties in the determination of the curvature values within flat triangles. We select 30 diametrical directions through the mass centre of the particle by equal spherical angles, including also the three principal dimensions for subsequent diametrical point loading. For comparing the breakage stress and energy between irregular and regular shaped particles, an ellipsoid with three principal dimensions equal to 2.6, 1.3 and 0.65 mm is also compressed by the same loading procedure of the LBS particle. The ellipsoid also has 1,280 triangular meshes over its surface generated by spherical harmonics.

Regarding the fracture patterns, there are three main types: chipping, two main fragments splitting, and three main fragments splitting. The patterns shown in Fig. 10 (a), (b) and (c) are taken from loading directions aligned with the maximum, median and minimum principal dimensions, respectively, of the particle shape during the crushing processes. Notably, the direction of the minimum dimension also coincides with experimental platen loading, which is also simulated and shown in Fig. 10 (d) as a comparison. The differences between fracture patterns in Fig. 10 (c) and (d), again confirm that a reduced contact curvature avoids stress concentration, while higher energy is needed for a major breakage thus causing more severe fracture patterns. This is consistent with the results of spherical particles, shown in Fig. 8 (a), regarding breakage for point and flat platen loads.

No main fracture surface is found through the whole particle in the chipping mode.

This is because the breakage stress is relatively small, which results in less energy to generate the fracture. By contrast, when compressed along the minimum dimension direction, the higher breakage stress contributes to increased fracture energy producing wider fractures and even up to three main fragments can be generated. The simulated fracture patterns are similar to relevant experiments in [50], except for the chipping mode. Considering that the LBS particle in their experiment is rotated in a smoothed drum and points of long diameters usually have high curvature values, it is difficult to compress it stably along with longer dimensions. As a result, the crushed particles are usually fractured along smaller dimensions in [50], thus leading to higher breakage stress similar platen loading tests and no chipping breakage mode.

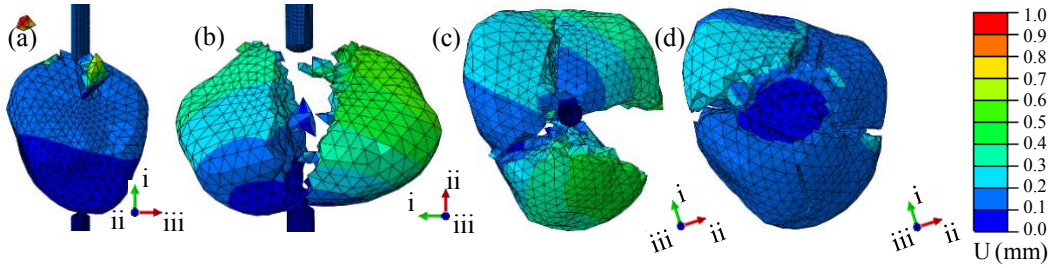

Fig. 10 Three types of fracture patterns due to rotational point loading: (a) chipping; (b) two main fragments splitting; (c) three main fragments splitting; (d) platen load towards minimum dimension (i, ii and iii denote maximum, median and minimum principal dimensions, respectively, of the intact LBS particle before compressed). Coloured by the scaler displacement, U.

4. Results and Discussion

Here, we focus on the statistical analyses and discussion of results correlating particle morphology with breakage behaviour.

4.1 Distributions of breakage stresses

The 30 cases of diametrical directional loading presented in Section 3.2 show distinct breakage behaviour. Fig. 11 depicts the cumulative distributions (a) and the Weibull distributions (b) of breakage stresses for the LBS and the ellipsoid particles. Evidently, even though both particles have the same material properties, the breakage stresses along the different diametrical directions are contrasting. The ellipsoid particle has an averaged breakage stress (10 MPa) much lower than LBS particle (20 MPa) and a larger stress variance, due to its more elongated shape. That may be the reason why LBS particle shapes are more likely to survive in sand assemblies rather than elongated ellipsoid-like shapes [51], because their directional strength is more stable and overall the whole particle can sustain higher stress conditions when pushed against one another. Interestingly, the Weibull modulus (4.4) of the distribution for rotational breakage stresses of the LBS particle is close to the value reported in experimental platen-loading-based breakage stresses of single quartz sand particles (e.g., 4.2 in [7]). The obvious difference here is that our simulations were conducted on only one identical sand particle, while the experiments were performed on multiple particles. The nearly identical Weibull modulus also implies that particle shape may also contribute to the variance of breakage stresses in addition to internal flaws.

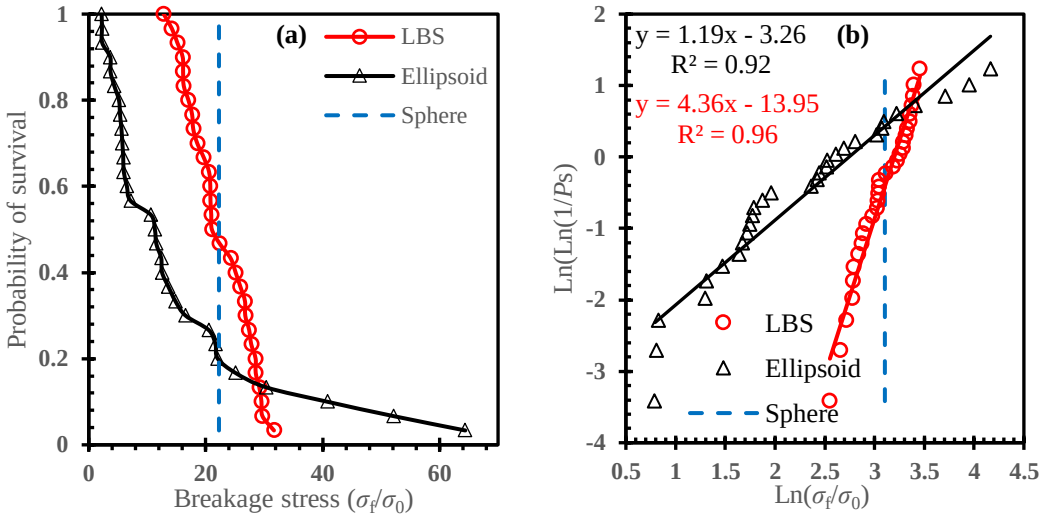

Fig. 11 Distributions of breakage stress of rotational point loading compression tests for the LBS and the ellipsoid particles: (a) Cumulative distributions; (b) Weibull distributions (σ_0=1MPa). The dashed vertical lines indicate the corresponding values for the equivalent-volume sphere.

4.2 Influences of curvature and loading distance

Apart from the commonly used maximum curvature (k_1), minimum curvature (k_2), average curvature ($k_M = (k_1+k_2)/2$) and Gaussian curvature ($k_g = k_1*k_2$) from their one-ring neighbourhood for 3D vertices [52-53], the curvedness ($k_C = \sqrt{(k_1^2 + k_2^2)/2}$) is considered here as an alternative measure from principal curvatures which avoid negative values found in k_1, k_2, k_M and k_g, and seamlessly combines two contact points. The combined curvedness is defined in similar manner to that of curvedness (k_C): $k_{com} = \sqrt{(k_{C1}^2 + k_{C2}^2)/2}$, where k_{C1} and k_{C2} are curvedness of two contact points.

Fig. 12 shows that the particle breakage stress is highly correlated with both

contact distances and the combined curvedness of two contact points, for both LBS and the ellipsoid particles. However, the 'diameters' would have some implicit correlation with the curvature values of their two end points for a given shape. Fig. 13 shows a general monotonic relationship between the diametrical length and corresponding normalised combined curvedness sweeping through the particle surfaces. Fig. 14 shows a 3D plot for breakage stress of rotational point loading compression, versus loading distance and its combined curvedness. It has been widely accepted that particle strength is size dependent and the correlation in log-log scales is linear [7]. For simplicity, the load distances (d) between two platens just before compression is usually considered as the particle sizes. From the FDEM simulations using rotational point loading tests, the breakage stresses are found to be linearly correlated with d in log-log scale for the same particle. Thereby, it seems that the so-called size effect may be due to variations of loading distances rather than the actual size.

Furthermore, the breakage stresses of point loading close to the minimum principal dimension directions are pointed out in Fig. 12 and among the highest values. In some cases, higher breakage stresses may be observed since another major influencing factor is the combined curvedness of the two diametrical contact points. Consequence of the above conclusion, traditional compression tests using platens somewhat overestimate the breakage stresses.

In the perspective of sand particle samples in continuum scale, their anisotropic fabric features are usually quantified by fabric tensors, and a popular directional fabric tensor is defined and based on the distribution of the principal dimension directions

[54]. Meanwhile, deformation-induced inhomogeneity of granular materials is also observed during the loading [55-56], also called yielding [57]. Therefore, the fracture criteria based on the shortest dimensions is not sufficient to assess the breakage behaviour of irregular particles within a granular assembly. At the grain scale, particle strengths depend on the contact direction, i.e., stress and fabric tensors, can be used to better describe the continuum breakage behaviour.

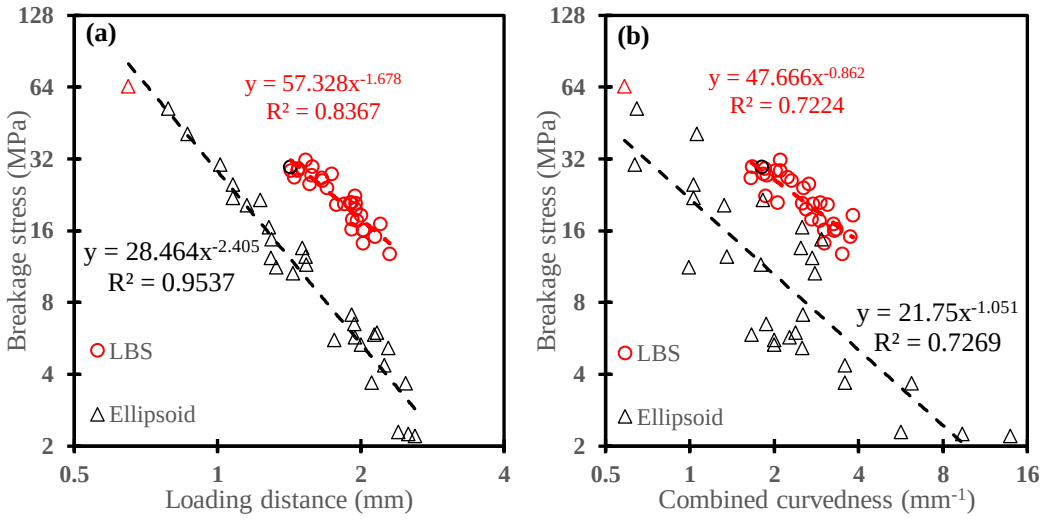

Fig. 12 Breakage stresses vs (a) loading distances and (b) combined curvedness for rotational diametrical point loading for the scanned LBS particle and an ellipsoid. (The corresponding red triangle and black circle represent point-loading tests towards the minimum dimensional directions for the ellipsoid and LBS particles.)

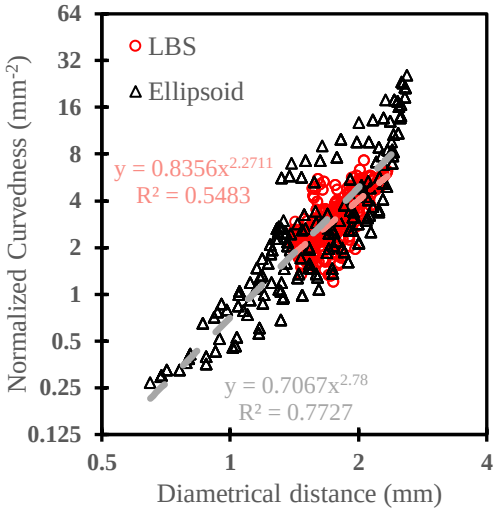

Fig. 13 Distributions of normalised curvedness multiplied by its corresponding diametrical distance versus 321 diametrical lengths crossing the mass centre for the LBS and ellipsoid particles

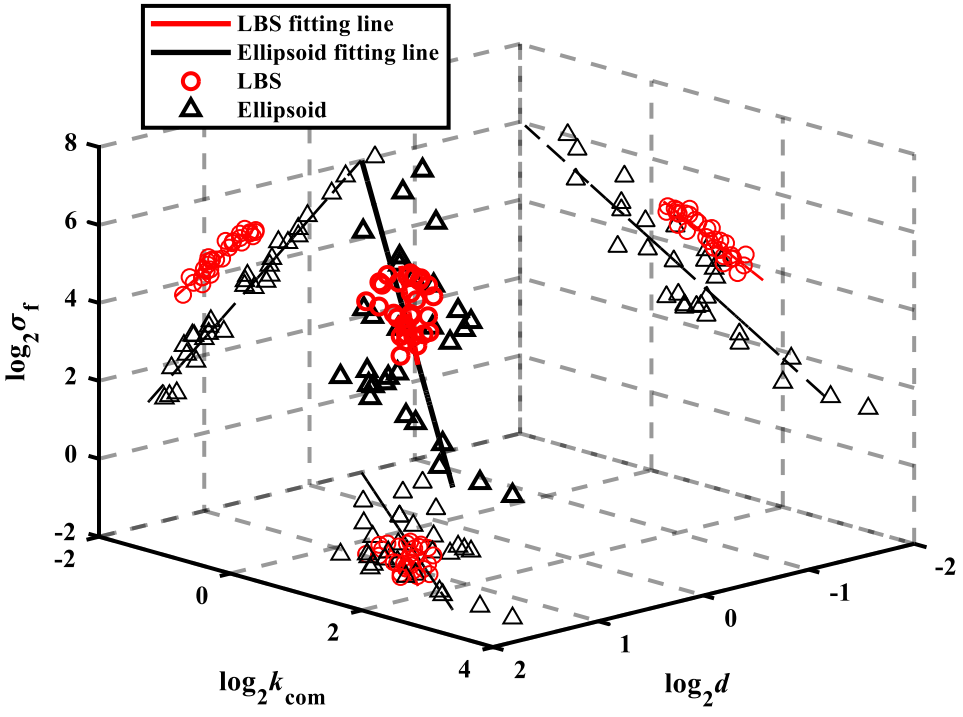

Fig. 14 Unique point-load-induced single particle breakage stress curve in logarithmic scale σ_f-k_{com}-d space

4.3 Energetic analysis of particle breakage

In geomechanics, energy evolution is the main concern of constitutive modelling in continuum scale [58-64]. In this section, the energy evolution during the breakage processes is analysed at the grain scale. In single particle crushing experiments two energy forms, namely input energy and fracture energy, can be retrieved. Input energy is calculated from load-displacement curves, while fracture energy is obtained from the newly created fracture surface areas, which are directly obtained from CT images [65-66]. Fig. 15 provides (a) input energy and (b) increased surface area of the experimental and simulated platen-loading of single particle breakage. During the severe breakage process, however, fragments may be too small for the resolution of CT images to accurately capture the total surface area. In addition, bigger internal cracks or flaws can also reduce accuracy of calculating surface area. While in FDEM simulations the cracked area is highly dependent on pre-existing CIEs, the size of which determines the smallest available fragments. That is the reason why discrepancies in terms of fracture area are found between experimental and simulation results, in particular for Scan 3 in the CT monitored experiments, shown in Fig. 15 (b). In contrast, for Scan 2 fewer fragments are generated and thus less affected by CT resolution in experiments and CIE size is found, demonstrating the capability of FDEM simulations.

In Fig. 16, four types of energy are analysed, namely maximum elastic strain energy (E_E), input energy by external works (E_W), damage energy (E_D), and friction energy (E_F) at the final stage with no load bearing capacity. In this study, the damage in CIEs is defined through (in Fig. 3):

$$\boldsymbol{\sigma}^{c} = (1-D^{'})\boldsymbol{\sigma}^{u}, \tag{15}$$

where $\boldsymbol{\sigma}^{u}$ is the undamaged stress and $D' \in [0,1]$ is the damage parameter. Thus the strain energy is

$$E_S = \int_0^t \left(\int_V \left(1-D^{'}\right)\boldsymbol{\sigma}^{u} : \dot{\varepsilon}^{el} dV \right) dt . \tag{16}$$

Simultaneously, the damage D' is time dependent and the strain energy (E_S) could be decomposed into the recoverable elastic energy (E_E) and damage-dissipated energy (E_D):

$$E_E = \int_0^t \left(\int_V \left(1-D_t^{'}\right)\boldsymbol{\sigma}^{u} : \dot{\varepsilon}^{el} dV \right) d\tau = \int_0^t \left(\int_V \frac{\left(1-D_t^{'}\right)}{\left(1-D^{'}\right)}\boldsymbol{\sigma}^{c} : \dot{\varepsilon}^{el} dV \right) dt , \tag{17}$$

$$E_D = \int_0^t \left(\int_V \left(D_t^{'}-D^{'}\right)\boldsymbol{\sigma}^{u} : \dot{\varepsilon}^{el} dV \right) d\tau = \int_0^t \left(\int_V \frac{\left(D_t^{'}-D^{'}\right)}{\left(1-D^{'}\right)}\boldsymbol{\sigma}^{c} : \dot{\varepsilon}^{el} dV \right) dt . \tag{18}$$

For explicit definition of friction energy (E_F), the surface traction vector ($\mathbf{t}$) can be split into surface normal load ($\mathbf{t}^{l}$) and frictional traction ($\mathbf{t}^{f}$) along boundary S. Then it can be written as

$$E_F = \int_0^t \left(\int_S \mathbf{v}\cdot\mathbf{t}^{f} dS \right) dt . \tag{19}$$

where $\mathbf{v}$ is the velocity field vector.

Except for the friction energy, all other 3 energy terms conform to Weibull distributions well in Fig. 16. Interestingly, regardless of the particle LBS particle or ellipsoid, the Weibull modulus of maximum elastic strain energy is evidently higher than those of other energy distributions; that is, with respect to the loading directions,

the maximum stored strain energy changes less than other energy types. Although the Weibull modulus of the maximum elastic strain energy for the LBS particle (7.3298) is slightly lower than that of the input energy (7.4427), the two values for the ellipsoid particle are 17.278 and 3.5808, respectively. The less variance in maximum elastic strain energy than the breakage stress implies that the stored maximum elastic strain energy can be a replacement as a breakage criterion. In particular, for regular-shaped particles, of which maximum elastic energy can be obtained analytically by integrating the Hertzian contact force for assessing the particle breakage [67-68]. We further compare the maximum E_E and E_D during the compression process of rotational point tests for both LBS and ellipsoid particles in Fig. 17, where the maximum E_E is significantly close to E_D for the 60 tests. Although in this study diametrical point load with less sliding or rotation in fracturing processes is applied, friction dissipation yet takes more parts of input energy than any other energy components, as illustrated in Table. 2. The sliding between fractured parts also contributes to the total friction energy. In continuum-scaled simulation of granular samples considering particle breakage [69-70], the ratio of friction dissipation to input energies is larger than that of point-load-induced single particle breakage due to the sliding of particles.

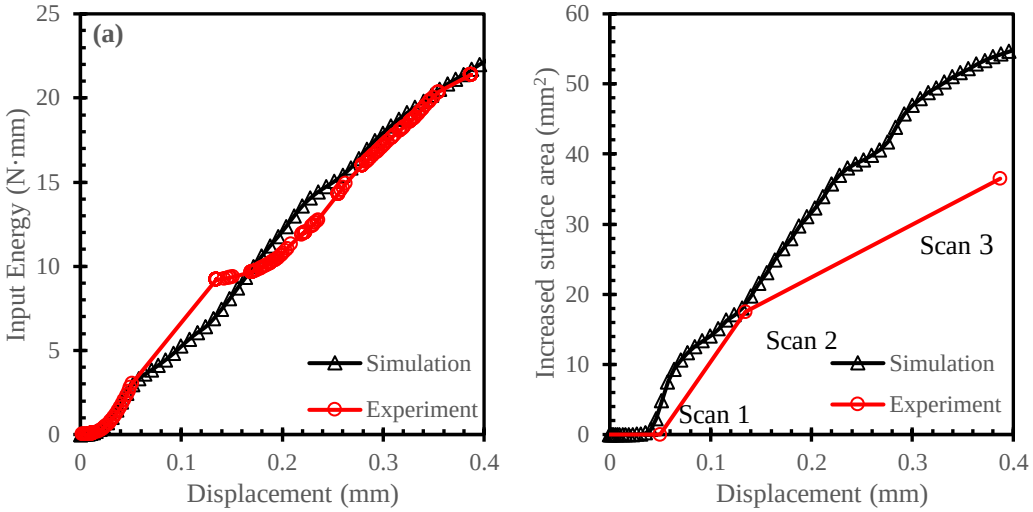

Fig. 15 (a) Correlation between input energy and (b) cumulatively increased surface area and displacement for experimental and simulated platen load tests in Fig. 1

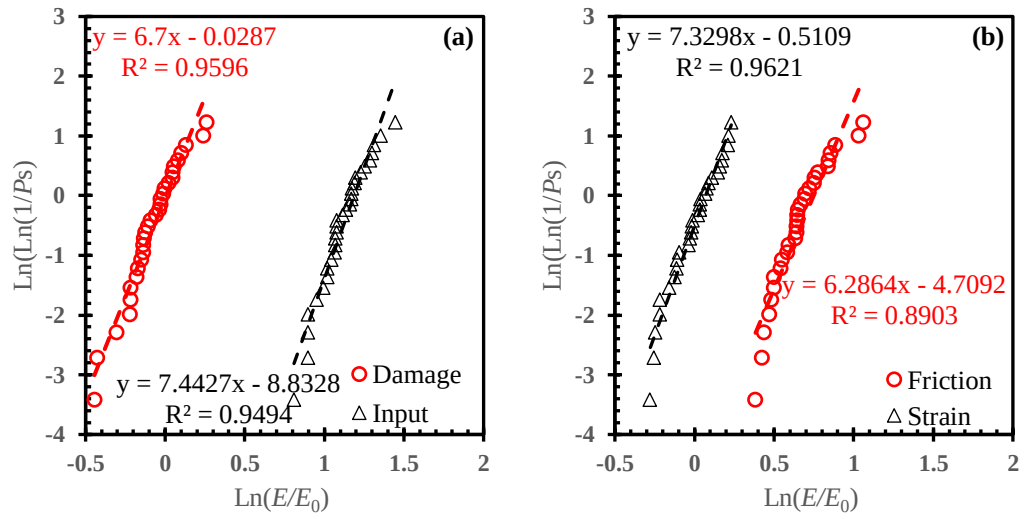

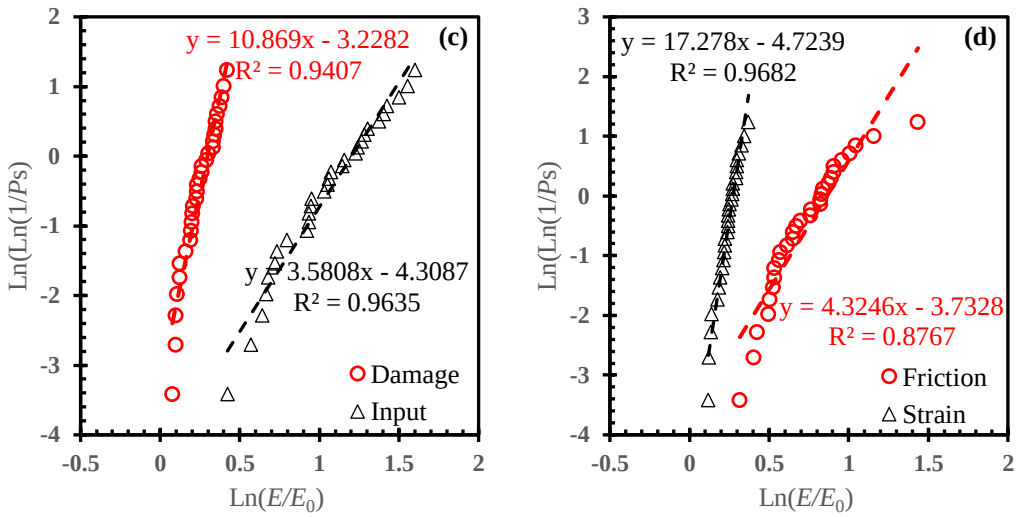

Fig. 16 Distributions of energy terms for rotational point load: Compression of LBS ((a) and (b)) and ellipsoid ((c) and (d)) particles (E_0=1N·mm)

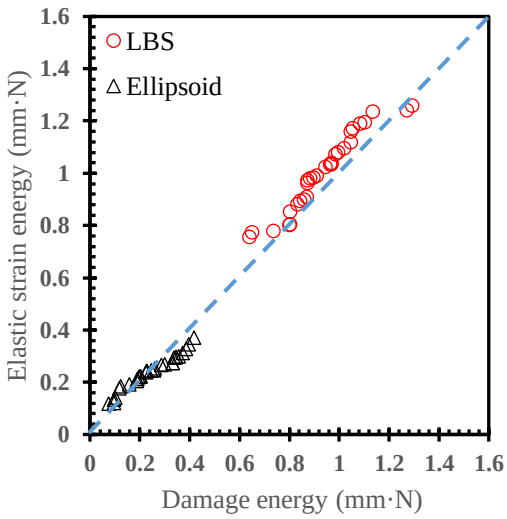

Fig. 17 The corelation between the maximum E_E and ultimate E_D for rotational point compression tests for the LBS and ellipsoid particles

Particle kind	(E_E/E_W)	(E_D/E_W)	(E_F/E_W)
LBS	0.3288	0.3071	0.6384
Ellipsoid	0.2378	0.2394	0.6918

Table. 2 Summary of average ratios of maximum E_E, E_D and E_F to E_W for LBS and ellipsoid particles

5. Conclusions

In this study, a combined FDEM approach has been adopted to simulate particle breakage behaviour emphasising on the particle shape effects. A CT-monitored experiment of a single particle crushing was taken as a benchmark and the analytical solution was verified. The main conclusions withdrawn from this study are as follows:

- The simulations of rotational point loading provide a powerful tool to assess the same non-spherical particle shapes with multiple breakage measurements that are impossible to study experimentally.
- Diametric-load-induced particle breakage behaviour, in terms of breakage stress and fracture patterns, is governed by both their loading distances and curvature at contact points. Therefore, the new breakage stress concept proposed based on load distance and curvedness at contact points provides an important reference for future numerical researches on single particle breakage.
- The maximum elastic strain energy during deformation was found to be an effective energy breakage criterion to determine strength of brittle particles.

These conclusions are generalised from three types of shapes investigated in this study, i.e., spheres of difference sizes, ellipsoids, and LBS particles, of which global morphology features are isotropic, symmetric and irregular, respectively. In a continuum-scaled particulate environment, since most fractured particles are in contact with more than two neighbour particles, it is necessary to consider the contribution of

all forces to the stored elastic strain energy in them. Care should be taken when taking critical elastic strain energy in the strength model as the sum of the strain energies of all contacts of a particle as a hypothesis and until experimental justification becomes possible. The results and findings in this study provide a promising way to unravel the dominating fracture mechanisms for irregular particles, and a conceptual numerical framework for particle breakage. It also enables future investigations to understand the behaviour of brittle granular media, and offers a new way to interpret the available experimental data regarding particle fracture behaviour.

ACKNOWLEDGEMENTS

The authors would like to acknowledge the support from the Australian Research Council through its Discovery Early Career Researcher Award (DE150101703) and ARC Project (DP170104192).

REFERENCES

[1] Coop, M. R., Sorensen, K. K., Bodas Freitas, T., & Georgoutsos, G. (2004). Particle breakage during shearing of a carbonate sand. *Géotechnique*, *54*(3), 157-163.

[2] Mook, W. M., Nowak, J. D., Perrey, C. R., Carter, C. B., Mukherjee, R., Girshick, S. L., ... & Gerberich, W. W. (2007). Compressive stress effects on nanoparticle modulus and fracture. *Physical Review B*, *75*(21), 214112.

[3] Yin, A., Yang, X., Yang, S., & Jiang, W. (2011). Multiscale fracture simulation of three-point bending asphalt mixture beam considering material heterogeneity. *Engineering Fracture Mechanics*, *78*(12), 2414-2428.

[4] Bažant, Z. P. (1984). Size effect in blunt fracture: concrete, rock, metal. *Journal of Engineering Mechanics*, *110*(4), 518-535.

[5] Bažant, Z. P., & Yavari, A. (2005). Is the cause of size effect on structural strength fractal or energetic–statistical?. *Engineering fracture mechanics*, *72*(1), 1-31.

[6] Weibull, W. (1951). Wide applicability. *Journal of applied mechanics*, *103*(730), 293-297.

[7] Nakata, A. F. L., Hyde, M., Hyodo, H., & Murata. (1999). A probabilistic approach to sand particle crushing in the triaxial test. *Géotechnique*, *49*(5), 567-583.

[8] Wang, W., & Coop, M. R. (2016). An investigation of breakage behaviour of single sand particles using a high-speed microscope camera. *Géotechnique*, *66*(12), 984-998.

[9] McDowell, G. R., Bolton, M. D., & Robertson, D. (1996). The fractal crushing of granular materials. *Journal of the Mechanics and Physics of Solids*, *44*(12), 2079-2101.

[10] Bartake, P. P., & Singh, D. N. (2007). A generalized methodology for determination of crushing strength of granular materials. *Geotechnical and Geological Engineering*, *25*(2), 203.

[11] Cavarretta, I., & O'sullivan, C. (2012). The mechanics of rigid irregular particles subject to uniaxial compression. *Géotechnique*, *62*(8), 681.

[12] McDowell, G. R., & Harireche, O. (2002). Discrete element modelling of soil particle fracture. *Géotechnique*, *52*(2), 131-135.

[13] Cil, M. B., & Alshibli, K. A. (2014). 3D evolution of sand fracture under 1D compression. *Géotechnique*, *64*(5), 351.

[14] Tapias, M., Alonso, E. E., & Gili, J. (2015). A particle model for rockfill behaviour. *Géotechnique*, *65*(12), 975-994.

[15] ISRM (International Society for Rock Mechanics). (1985). Suggested method for determining point load strength. *International Journal of Rock Mechanics and Mining Science, Abstract* (22), 51-60.

[16] Hiramatsu, Y., & Oka, Y. (1966, May). Determination of the tensile strength of rock by a compression test of an irregular test piece. In *International Journal of Rock Mechanics and Mining Sciences & Geomechanics Abstracts* (Vol. 3, No. 2, pp. 89-90). Pergamon.

[17] Chau, K. T., & Wei, X. X. (1999). Spherically isotropic, elastic spheres subject to diametral point load strength test. *International journal of solids and structures*, *36*(29), 4473-4496.

[18] Pejchal, V., Žagar, G., Charvet, R., Dénéréaz, C., & Mortensen, A. (2017). Compression testing spherical particles for strength: Theory of the meridian crack test and implementation for microscopic fused quartz. *Journal of the Mechanics and Physics of*

Solids, *99*, 70-92.

[19] Russell, A. R., & Wood, D. M. (2009). Point load tests and strength measurements for brittle spheres. *International Journal of Rock Mechanics and Mining Sciences*, *46*(2), 272-280.

[20] Zhao, B., Wang, J., Coop, M. R., Viggiani, G., & Jiang, M. (2015). An investigation of single sand particle fracture using X-ray micro-tomography. *Géotechnique*, *65*(8), 625-641.

[21] Zhu, F., & Zhao, J. (2018). A peridynamic investigation on crushing of sand particles. *Géotechnique*, 1-15.

[22] Cavarretta, I., O'Sullivan, C., & Coop, M. R. (2016). The relevance of roundness to the crushing strength of granular materials. *Géotechnique*, *67*(4), 301-312.

[23] Brzesowsky, R. H., Spiers, C. J., Peach, C. J., & Hangx, S. J. T. (2011). Failure behavior of single sand grains: theory versus experiment. *Journal of Geophysical Research: Solid Earth*, *116*(B6).

[24] Cheng, Y. P., Nakata, Y., & Bolton, M. D. (2003). Discrete element simulation of crushable soil. *Geotechnique*, *53*(7), 633-641.

[25] Hanley, K. J., O'Sullivan, C., Oliveira, J. C., Cronin, K., & Byrne, E. P. (2011). Application of Taguchi methods to DEM calibration of bonded agglomerates. *Powder technology*, *210*(3), 230-240.

[26] Lobo-Guerrero, S., & Vallejo, L. E. (2005). Discrete element method evaluation of granular crushing under direct shear test conditions. *Journal of Geotechnical and Geoenvironmental Engineering*, *131*(10), 1295-1300.

[27] de Bono, J. P., & McDowell, G. R. (2018). Micro mechanics of drained and undrained shearing of compacted and overconsolidated crushable sand. *Géotechnique*.

[28] Ciantia, M. O., Arroyo, M., O'Sullivan, C., Gens, A., & Liu, T. (2018). Grading evolution and critical state in a discrete numerical model of Fontainebleau sand. *Géotechnique*, 1-15.

[29] Andrade, J. E., Lim, K. W., Avila, C. F., & Vlahinić, I. (2012). Granular element method for computational particle mechanics. *Computer Methods in Applied Mechanics and Engineering*, *241*, 262-274.

[30] Kawamoto, R., Andò, E., Viggiani, G., & Andrade, J. E. (2016). Level set discrete element method for three-dimensional computations with triaxial case study. *Journal of the Mechanics and Physics of Solids*, *91*, 1-13.

[31] Kawamoto, R., Andò, E., Viggiani, G., & Andrade, J. E. (2018). All you need is shape: Predicting shear banding in sand with LS-DEM. *Journal of the Mechanics and Physics of Solids*, *111*, 375-392.

[32] Nadimi, S., & Fonseca, J. (2017). A micro finite-element model for soil behaviour. *Géotechnique*, *68*(4), 290-302.

[33] Druckrey, A. M., & Alshibli, K. A. (2016). 3D finite element modeling of sand particle fracture based on in situ X-Ray synchrotron imaging. *International Journal for Numerical and Analytical Methods in Geomechanics*, *40*(1), 105-116.

[34] Abaqus 6.14–1, (2014): Analysis user's Manual. Providence, USA.

[35] Gonzalez, R. C. and Woods, R. E. (2010). Digital image processing. Upper Saddle River, N.J.: Pearson/Prentice Hall.

[36] Wei, D., Wang, J., Nie, J., & Zhou, B. (2018). Generation of realistic sand particles with

fractal nature using an improved spherical harmonic analysis. *Computers and Geotechnics*, *104*, 1-12.

[37] Press, W. H., Teukolsky, S. A., Vetterling, W. T., & Flannery, B. P. (1992). *Numerical recipies in C* (Vol. 2). Cambridge: Cambridge university press.

[38] Imseeh, W. H., & Alshibli, K. A. (2018). 3D finite element modelling of force transmission and particle fracture of sand. *Computers and Geotechnics*, *94*, 184-195.

[39] Barenblatt, G. I. (1959). Equilibrium cracks formed during brittle fracture rectilinear cracks in plane plates. *Journal of Applied Mathematics and Mechanics*, *23*(4), 1009-1029.

[40] Hillerborg, A., Modéer, M., & Petersson, P. E. (1976). Analysis of crack formation and crack growth in concrete by means of fracture mechanics and finite elements. *Cement and concrete research*, *6*(6), 773-781.

[41] Xu, X. P., & Needleman, A. (1996). Numerical simulations of dynamic crack growth along an interface. *International Journal of Fracture*, *74*(4), 289-324.

[42] Guo, L., Xiang, J., Latham, J. P., & Izzuddin, B. (2016). A numerical investigation of mesh sensitivity for a new three-dimensional fracture model within the combined finite-discrete element method. *Engineering Fracture Mechanics*, *151*, 70-91.

[43] Wu, Z., Ma, L., & Fan, L. (2018). Investigation of the characteristics of rock fracture process zone using coupled FEM/DEM method. *Engineering Fracture Mechanics*, *200*, 355-374.

[44] Benzeggagh, M. L., & Kenane, M. J. C. S. (1996). Measurement of mixed-mode delamination fracture toughness of unidirectional glass/epoxy composites with mixed-mode bending apparatus. *Composites science and technology*, *56*(4), 439-449.

[45] Turon, A., Davila, C. G., Camanho, P. P., & Costa, J. (2007). An engineering solution for mesh size effects in the simulation of delamination using cohesive zone models. *Engineering fracture mechanics*, *74*(10), 1665-1682.

[46] Lens, L. N., Bittencourt, E., & d'Avila, V. M. (2009). Constitutive models for cohesive zones in mixed-mode fracture of plain concrete. *Engineering Fracture Mechanics*, *76*(14), 2281-2297.

[47] Tatone, B. S., & Grasselli, G. (2015). A calibration procedure for two-dimensional laboratory-scale hybrid finite–discrete element simulations. *International Journal of Rock Mechanics and Mining Sciences*, *75*, 56-72.

[48] Turcotte, D. L. (1986). Fractals and fragmentation. *Journal of Geophysical Research: Solid Earth*, *91*(B2), 1921-1926.

[49] Nagahama, H. (1993, August). Fractal fragment size distribution for brittle rocks. In *International journal of rock mechanics and mining sciences & geomechanics abstracts* (Vol. 30, No. 4, pp. 469-471). Pergamon.

[50] Wang, W., & Coop, M. R. (2018). Breakage behaviour of sand particles in point-load compression. *Géotechnique Letters*, *8*(1), 61-65.

[51] Altuhafi, F. N., & Coop, M. R. (2011). Changes to particle characteristics associated with the compression of sands. *Géotechnique*, *61*(6), 459.

[52] Dong, C. S., & Wang, G. Z. (2005). Curvatures estimation on triangular mesh. *Journal of Zhejiang University-Science A*, *6*(1), 128-136.

[53] Zhao, B., & Wang, J. (2016). 3D quantitative shape analysis on form, roundness, and compactness with μCT. *Powder technology*, *291*, 262-275.

[54] Oda, M. (1982). Fabric tensor for discontinuous geological materials. *Soils and Foundations*, *22*(4), 96-108.

[55] Fonseca, J., O'Sullivan, C., Coop, M. R., & Lee, P. D. (2013). Quantifying the evolution of soil fabric during shearing using directional parameters. *Géotechnique*, *63*(6), 487-499.

[56] Fonseca, J., Nadimi, S., Reyes-Aldasoro, C. C., & Coop, M. R. (2016). Image-based investigation into the primary fabric of stress-transmitting particles in sand. *Soils and Foundations*, *56*(5), 818-834.

[57] McDowell, G. R., & Bolton, M. D. (1998). On the micromechanics of crushable aggregates. *Géotechnique*, *48*(5), 667-679.

[58] Oldecop, L. A., & Alonso, E. E. (2007). Theoretical investigation of the time-dependent behaviour of rockfill. *Géotechnique*, *57*(3), 289-301.

[59] Einav, I. (2007). Breakage mechanics—part I: theory. *Journal of the Mechanics and Physics of Solids*, *55*(6), 1274-1297.

[60] Einav, I. (2007). Breakage mechanics—Part II: Modelling granular materials. *Journal of the Mechanics and Physics of Solids*, *55*(6), 1298-1320.

[61] Russell, A. R., & Einav, I. (2013). Energy dissipation from particulate systems undergoing a single particle crushing event. *Granular Matter*, *15*(3), 299-314.

[62] Zhang, Y. D., Buscarnera, G., & Einav, I. (2015). Grain size dependence of yielding in granular soils interpreted using fracture mechanics, breakage mechanics and Weibull statistics. *Géotechnique*, *66*(2), 149-160.

[63] Zhang, Y. D., & Buscarnera, G. (2015). Prediction of breakage-induced couplings in unsaturated granular soils. *Géotechnique*, *65*(2), 135-140.

[64] Zhang, Y. D., & Buscarnera, G. (2017). A rate-dependent breakage model based on the kinetics of crack growth at the grain scale. *Géotechnique*, *67*(11), 953-967.

[65] Landis, E. N., Nagy, E. N., & Keane, D. T. (2003). Microstructure and fracture in three dimensions. *Engineering Fracture Mechanics*, *70*(7-8), 911-925.

[66] Sufian, A., & Russell, A. R. (2013). Microstructural pore changes and energy dissipation in Gosford sandstone during pre-failure loading using X-ray CT. *International Journal of Rock Mechanics and Mining Sciences*, *57*, 119-131.

[67] Zhao, S., Gan, Y., Kamlah, M., Kennerknecht, T., & Rolli, R. (2013). Influence of plate material on the contact strength of Li4SiO4 pebbles in crush tests and evaluation of the contact strength in pebble–pebble contact. *Engineering Fracture Mechanics*, *100*, 28-37.

[68] Annabattula, R. K., Kolb, M., Gan, Y., Rolli, R., & Kamlah, M. (2014). Size-dependent crush analysis of lithium orthosilicate pebbles. *Fusion Science and Technology*, *66*(1), 136-141.

[69] Wang, J., & Yan, H. (2012). DEM analysis of energy dissipation in crushable soils. *Soils and Foundations*, *52*(4), 644-657.

[70] Ma, G., Zhou, W., Chang, X. L., & Chen, M. X. (2016). A hybrid approach for modeling of breakable granular materials using combined finite-discrete element method. *Granular Matter*, *18*(1), 7.

[71] Ma, G., Zhang, Y., Zhou, W., Ng, T. T., Wang, Q., & Chen, X. (2018). The effect of different fracture mechanisms on impact fragmentation of brittle heterogeneous solid. *International Journal of Impact Engineering*, *113*, 132-143.

[72] Ma, G., Zhou, W., Zhang, Y., Wang, Q., & Chang, X. (2018). Fractal behavior and shape

characteristics of fragments produced by the impact of quasi-brittle spheres. *Powder Technology*, *325*, 498-509.